WAKE FLOW DYNAMICS OF AN A320 MORPHING WING PROTOTYPE THROUGH TIME-RESOLVED PIV AND HI-FI SIMULATIONS

Mateus Carvalho[1,2], Jacques Abou-Khalil[4,1], Clément Rouaix[1,2], Abderahmane Marouf[1,3], Horia Hangan[2], J.F. Rouchon[4], M. Braza[1]

[1]Institut de Mécanique des Fluides de Toulouse (IMFT) UMR 5502 CNRS-INPT-UT3
[2]Faculty of Engineering and Applied Science (FEAS), Ontario Tech University
[3]ICUBE Laboratoire des sciences de l'Ingénieur, de l'Informatique et de l'Imagerie, UMR 7357 CNRS-Univ.Strasbourg-ENGEES-INSA
[4]LAPLACE Laboratoire Plasma et Conversion d'Energie, UMR 5213 CNRS-INPT-UT3

ABSTRACT

The present article investigates the electroactive morphing effects on the aerodynamic performance around an A320 wing prototype with an embedded system of near trailing edge piezoactuators able to vibrate and apply slight deformations at optimal frequencies and amplitudes. Physical experiments based on time-resolved PIV and Hi-Fi numerical simulations at Reynolds number of 1 million, incidence of 10° and Mach number of 0.06, corresponding to the low subsonic regime at take-off conditions, investigated the physical mechanisms related to the increase in lift, drag and noise source reduction, based on the modification of the turbulence structure along the shearing regions and its interaction with coherent structures in the near wake. A lift-to-drag increase in the order of 6% as well as a spectral energy reduction in the order of 15% in dB have been obtained for a specific range of the actuation frequency and for low vibration amplitude of $0.7\,mm$. The physical mechanisms related to these performances are analysed by spectral analysis and POD.

INTRODUCTION

This article is a detailed investigation with new results since the H2020 N°723402 EU research project "SMS"-"Smart Morphing & Sensing for aeronautical configurations", http://smartwing.org/SMS/EU,https://cordis.europa.eu/project/id/723402), coordinated by the Institut de Mécanique des Fluides de Toulouse, (IMFT), whose research is continuing in the ongoing National (French) research project "EMBIA", "Electrical Multiscale Bio-inspired Live-skin interfaces in Aeronautics" https://anr.fr/Project-ANR-21-CE05-0006, also coordinated by IMFT. Both projects are in strong collaboration with AIRBUS. These projects are the fruit of a multidisciplinary strong synergy during the last fifteen years between the IMFT and the LAPLACE-Laboratoire Plasma & Conversion d'Energie in Toulouse. In this collaboration Ontario Tech University in Canada has also been involved since 2022. In the context of the SMS-EU project, efficient morphing wing prototypes have been constructed and studied experimentally and numerically by the research team of IMFT-LAPLACE, including the so-called "hybrid electroactive morphing", able to operate at different time and length scales, as required by the turbulence spectrum nature, (Scheller 2015 and Scheller et al (2016)). The investigation of the morphing concepts and performances in all flight phases in the context of this project is provided in the book by Braza *et al,* 2023. In the present study, emphasis is attributed in a large parametric space of the vibration frequency applied in the near-trailing edge area by means of Hi-Fi simulations and new refined physical experiments. A discussion is provided on the morphing effects on the turbulence structure along the shearing regions and its influence on the aerodynamic performances.

EXPERIMENTAL SET-UP

The experiments have been carried out in the low-subsonic wind tunnel S4 of IMFT with an upstream velocity of $U_\infty = 21.5\,m/s$, corresponding to Reynolds and Mach numbers of $Re = 1 \times 10^6$ and $Ma = 0.063$, respectively. The so-called "Reduced Scale" - "RS" A320 morphing prototype of the SMS project has been used, having a chord of $c = 70\,cm$ and a span of $s = 60\,cm$. The wing is mounted with an angle of attack of $\alpha = 10°$, corresponding to a typical take-off configuration, in the S4 subsonic wind tunnel of IMFT, characterized by a 0.1% inlet turbulence intensity level. The aerodynamic balance, designed by LAPLACE provides an accuracy in the order of 0.01%.

MFC ("Micro-Fiber Composite") piezoelectric actuators have been embedded in the trailing-edge region figure 1. Each of them forms patches of length $L_p = 3.5\,cm$, (corresponding to 5% of the chord) and provide vibration amplitudes up to $a_p = 1\,mm$ by means of specific electrical alimentations, studied by the LAPLACE Laboratory, that actuate the piezos through an electric tension in the range of [800-1000] V. These parameters have been used according to optimization from previous studies on this prototype within the SMS project.

Regarding the Time-Resolved PIV (TRPIV) measurements, the interrogation window was located downstream of the trailing edge to investigate the shear layers dynamics. A "LaVision" camera model V2012 with a sampling frequency of $f_s = 10\,kHz$ was used for image acquisition. The tests were carried out at Reynolds numbers of $Re = 0.7 \times 10^6$ and $Re = 1 \times 10^6$. For particle tracking, correlation between consecutive snapshots was made using 1200×800 elements, each with a resolution of 16×16 pixels. LaVision software DaVis and Matlab were used for data processing. During the experiments, the velocity variation was less than 1.5%. For Tomographic PIV, four LaVision V2020 cameras were mounted on a custom-built experimental bench as shown in figure 2. The spanwise length of the measuring volume was $15\,mm$. The sampling frequency was $f_s = 10\,kHz$. 200,000 snapshots were captured. This Tomographic PIV campaign represents a first 3D velocity field database for morphing wings in the present Reynolds number range.

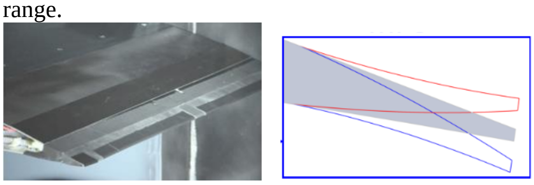

Figure 1. View of the near trailing-edge vibration and slight deformation: A320 morphing prototype. Tailing edge actuation obtained through MFC piezoactuators (Scheller 2015, Jodin *et al,* 2017).

NUMERICAL SIMULATIONS AND TURBULENCE MODELLING

The vibration and slight deformation of the near trailing edge region in numerical simulations exactly reflect the actuation obtained with MFC patches in experiments. The motion and deformation of the near trailing edge region produces a mesh deformation, which is taken into account in the NSMB (Navier Stokes Multi-Block) code (Hoarau *et al,* 2016*)* by using the Arbitrary Lagrangian Eulerian (ALE)

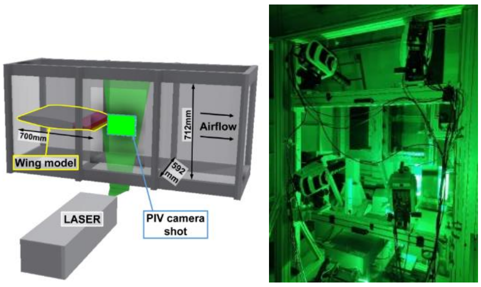

Figure 2. Experimental set-up in the S4 wind tunnel of IMFT. Left: Time-Resolved PIV (TRPIV) with image acquisition frequency of $10\,kHz$. Right: 4D Tomo-PIV with acquisition frequency of $10\,kHz$.

approach, Donea et al. 1982. A view of the grid deformation is seen in figure 3. An adapted turbulence modelling approach sensitized to accurately simulate coherent structures development in interaction with the chaotic turbulence, the Organised Eddy Simulation (OES), has been used (Braza et al. 2006, Bourget et al. 2008 and Szubert et al. 2015). This approach, not intrinsically 3D, allowed realization of a very large parametric study in respect of the vibration frequency. Furthermore, the DDES-OES (Delayed Detached Eddy Simulation with embedded Organised Eddy Simulation) approach in the near region (Haase *et al*, 2009), Simiriotis (2020), Marouf (2020) has been used for selected 3D cases.

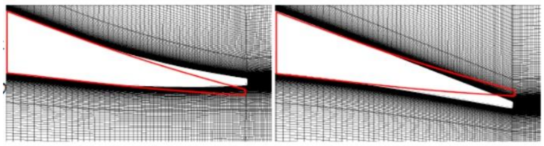

Figure 3. Slight deformation of the near-trailing-edge area and zoom of the computational grid.

RESULTS

Numerical Study

The three-dimensional flow structure for the non-actuated (static) case is shown in figure 4. The separation area and the shear layers mixing with the turbulence structures in the wake (blue regions) are illustrated, as well as very small-scale vortices in the boundary layer, thanks to a 60 million grid. A large parametric study on the amplitudes and vibration frequencies was carried out during the SMS project indicating the optimal actuation ranges. It was shown that amplitudes higher than $2\,mm$ lead to increase of drag. Therefore, the overall study in the present article focuses on vibration amplitudes (peak-to-valley) in the order of $0.7\,mm$, in both, experiments and simulations. As for the vibration frequencies, initial optimal ranges were found in the interval of $(100 - 300)\,Hz$ (Simiriotis *et al* 2019). In the present study, a lower range between $(40 - 80)\,Hz$ has been investigated and, as will be shown, provides a good aerodynamic performance increase. The fact that coherent structure dynamics in flows around bodies have predominant 2D characteristics allows for a first approximation of a 2D numerical investigation that makes possible the realisation of a large parametric study. Figure 5 (left) shows the vortex dynamics in the near region around the wing and in the intermediate area of the wake. The separation region (blue area) is illustrated as well as the formation of the upper and lower shear layers yielding to the alternating vortex shedding farther downstream. The mixing from each of these of these shear

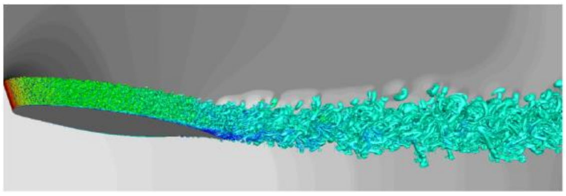

Figure 4. Q criterion coloured by pressure around the A320 RS wing prototype of the SMS project. Visualisation of the turbulence structure in the static (non-morphing) case using the DDES-OES approach and a 60 Million grid and spanwise length of one chord. The blue area shows the separated region and the shear layers turbulence mixing.

layers into the alternating eddies is clearly shown, as well as the Kelvin-Helmholtz vortices. By tracking the coherent vortices, it was found that the upper shear layer natural frequency (f_{USL}) is in the order of $130\,Hz$ and the lower shear layer one (f_{LSL}) in the order of $210\,Hz$. The von Kármán frequency (f_{VK}) is in the range of $(150 - 160)\,Hz$. Due to the interaction with the chaotic turbulence in the present Reynolds number range, these predominant frequencies form "bumps" in the energy spectrum as shown in figure 7 and are not distinct sharp peaks.

Figure 5 (right) shows an actuated case with vibration at $300\,Hz$. This frequency, close to the natural lower shear layer one, was found to reinforce this shear layer vortices by strengthening their vorticity magnitude and simultaneously by reducing their diffusion rate thanks to a shear-sheltering mechanism, thus providing a thinner near wake width. This mechanism is an "eddy-blocking" effect thanks to generation of smaller-scale vortices due to the actuation that interact with the existing turbulence and increase the momentum in the shear layers, pushing the regime towards a more supercritical one. This mechanism, first investigated in interfacial shear layers by Da Silva *et al.* (2014) has been thoroughly investigated along the studies of the multidisciplinary team IMFT-LAPLACE, (Jodin *et al* 2017), Marouf (2020), Szubert et al (2015), Tô *et al* (2019), Abou-Khalil *et al.* (2024), the three last corresponding to cruise conditions (inlet Mach number of 0.78).

Figure 5 (bottom-left) shows the 3D turbulence structure in the static case where spanwise undulations with well-distinct wavelengths are formed due to secondary instability amplification. These undulated vortex rows form specific junctions, vortex dislocations, along the span as analysed by DNS by Braza *et al* (2001). Figure 5 (right) shows the modification of this turbulence structure thanks to a morphing with vibration frequency of $300\,Hz$. There is a regularization of the streamwise vorticity that considerably attenuates the secondary instability. These facts, related to the wake thinning, have an immediate *feedback effect* in the wall pressure distribution yielding considerable benefits in the aerodynamic performances as shown in next paragraphs.

Figure 6 shows a good agreement between the simulations and the experiments that are detailed in next section.

Figure 7 shows the Power Spectral Density (PSD) in the near trailing-edge area. A considerable decrease of the frequency bump formed by the lower shear layer frequency has been obtained. In addition to the corresponding noise sources reduction, a *substantial increase of the lift coefficient* of 7.98% has been evaluated for an actuation frequency of $210\,Hz$ comparing to the static case by our numerical simulations.

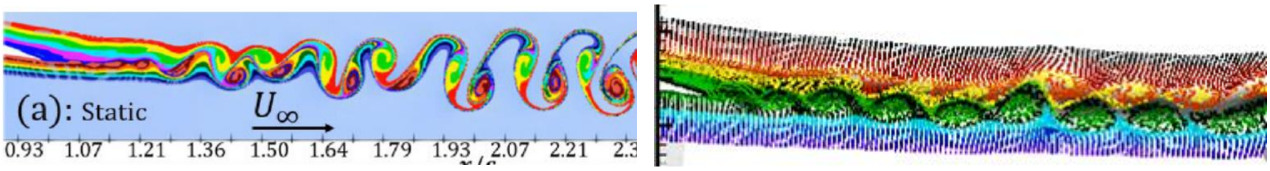

Figure 5. Numerical simulations. Top-left: static case, A320 RS wing prototype of the SMS project. Separation region formation beyond 0.8% of the chord followed by the upper and lower shear layers containing Kelvin-Helmholtz (KH) eddies, creating the von Kármán (VK) vortex street farther downstream.

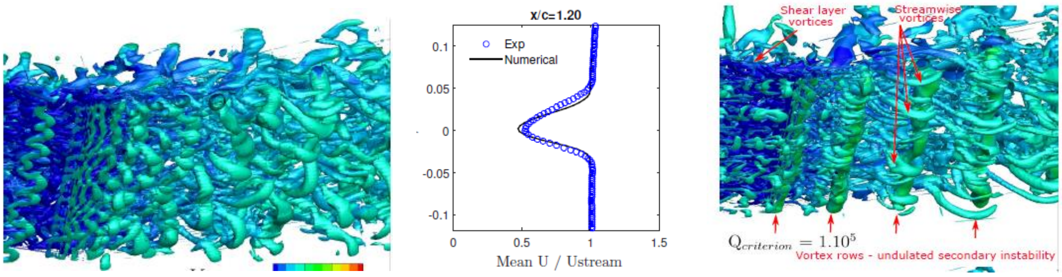

Figure 6. DDES-OES simulations; left: static case: formation of secondary instability and vortex dislocations (VL); middle: comparison of the simulations with the experiments - mean velocity profile in the near wake. Right: morphing with 300 Hz vibration: regularisation of the 3D vortex rows and suppression of VL.

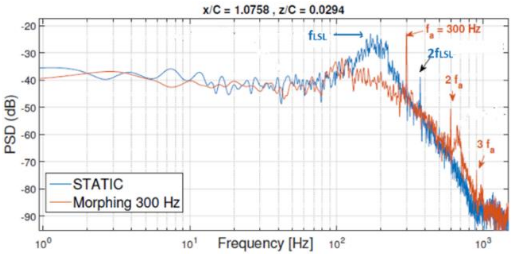

Figure 7. PSD at a point near the trailing-edge showing the natural lower shear layer frequency (f_{LSL}) bump in the range of (180 - 250) Hz in blue colour (static case) and its considerable reduction due to morphing at 300 Hz.

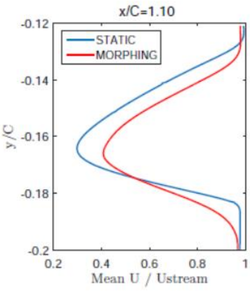

Figure 8. Mean longitudinal velocity profiles (absolute values) showing the reduction of the wake's width (static case in blue and morphing at 300 Hz in red).

These mechanisms have been analysed by means of the Proper Orthogonal Decomposition thanks to long series of snapshots generated by the numerical simulations as well as by the experiments discussed in a next paragraph. According to the POD, a decomposition of each physical quantity (in the present case the velocity field) to a number of shape modes multiplied by their corresponding temporal coefficients thanks to resolution of an eigenvalue problem (Berkooz *et al*, 1993) and under the hypothesis of the separable POD in time-space (Sirovich, 1987). The velocity field can be decomposed as following:

$$\vec{u}(\vec{x},t) = \sum^{\infty} a_n \vec{\Phi}_n(\vec{x})$$

where the temporal coefficients are:

$$a_k = \iint_{\Omega} u_i(x,t)\Phi_i^*(x)dxdt$$

determined by a set of eigenvalues, $\overline{a_k a_k} = \delta_{kk}\lambda_k$ through correlation matrix. Φ^* is the transpose of the matrix Φ.

Figure 9 shows the energy distribution of the POD modes for the static and morphing at 210 Hz. For this representation, the temporal average has been removed from each snapshot, therefore the decomposition provides the fluctuation effects. It is shown that the morphing decreases the energy beyond the 8th POD mode as well as the POD reconstruction with the first 10 modes according to the following relation, where the mean field has been added:

$$U(\vec{X},t) = \overline{U}(\vec{X}) + u'(\vec{X},t) = \overline{U}(\vec{X}) + \sum_{n=2}^{N} a_n(t)\Phi_n(\vec{X})$$

The reinforcement of the lower shear layer is shown in figure 10, associated to the evaluated lift increase to 7.98%, together with the weakening of the VK shedding.

Furthermore, the POD allows for *phasing* every snapshot in its corresponding phase angle in respect of the vortex shedding and for evaluation of the *phase-averaging fields in a period*. Through the two first POD modes, a phase angle for each snapshot can be derived according to the method by Perrin (2005) and under the following relation: $\Phi = \text{atan}\left(\frac{\sqrt{2\,\lambda_3}}{\sqrt{2\lambda_2}}\frac{a_2}{a_3}\right)$

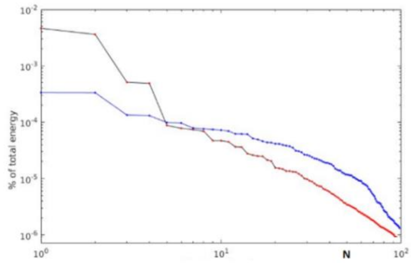

Figure 9. Energy distribution of the POD modes; blue: static, red: morphing at 210 Hz.

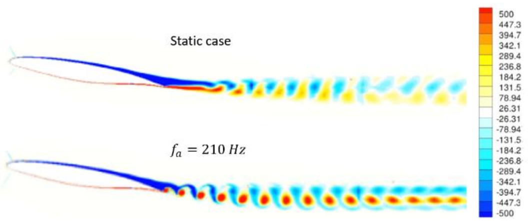

Figure 10. POD reconstruction with modes 1-10. Top: static, Bottom: morphing at 210 Hz.

The phase diagram is divided in a number of classes and each snapshot "drops" in its corresponding class that permits afterwards calculation of the phase-average in each class (figure 11). In the static case, the phase diagram indicates a predominant effect of the periodic VK vortex shedding. The dispersion comparing to a theoretical ‘one single ellipsis’ curve is due to the interaction with the other flow instabilities as for example the Kelvin-Helmholtz (KH) vortices, as well as to the influence of the multitude of chaotic processes depicted in the continuous frequency range of the PSD previously shown. The morphing (figure 12) shows a regularisation effect of this smearing through the reinforcement of the lower shear layer and decrease of the POD energy beyond an order of 10th mode previously shown.

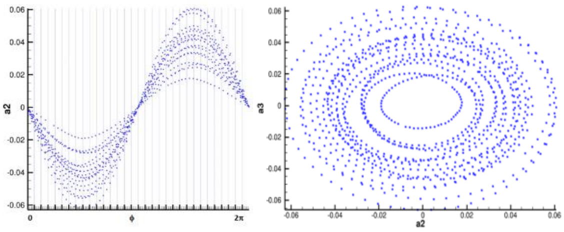

Figure 11. Evolution of the second mode temporal coefficient versus the phase-angle (left); phase diagram of the 3rd mode versus the 2nd one: effect of the periodic vortex shedding and its “smearing” due to the chaotic turbulence effects (right).

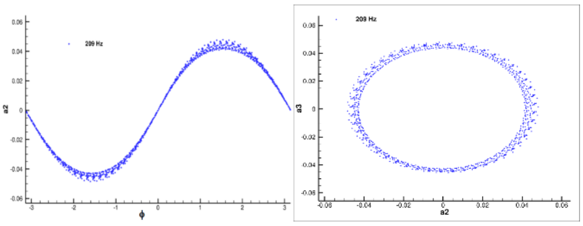

Figure 12. Idem as in figure 11 for the morphing case with vibration frequency of $209\,Hz$, showing attenuation of the phase-average spreading and the morphing ability to regularise the flow dynamics towards a more coherent pattern.

Regarding the aerodynamic performances, figure 13 shows interesting vibration frequency ranges indicated by red rectangles for the drag and lift mean coefficients and for their respective *rms*, minimal in these ranges that are explored through the experimental study as follows.

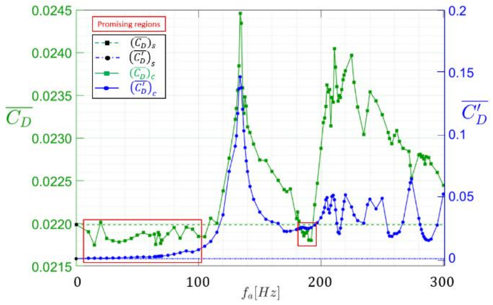

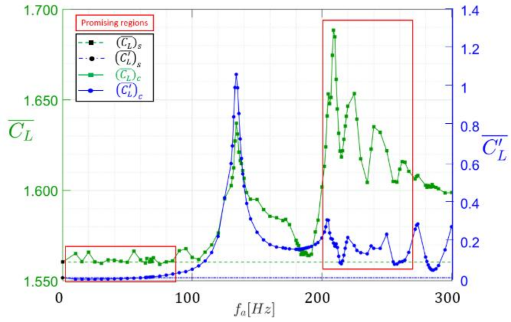

Figure 13. Mean drag and lift coefficients at different actuation frequencies (green) and their *rms* values (blue). Red rectangles indicate optimal regions including the frequencies in the ranges around $40\,Hz$ and $210\,Hz$.

Experimental Results

The PIV experiments (Time-Resolved and Tomo), as well as the electronics set-up for the piezoactuation have been conducted in the S4 wind tunnel of IMFT with the contribution of the “Signal & Image processing” team of the Institute, S. Cazin, M. Marchal and Hervé Ayroles. Figure 14 shows the mean velocity field at $Re = 500{,}000$ obtained by 4D Tomo-PIV for the static and morphing cases at $f_a = 300\,Hz$, illustrating a reduction of the velocity deficit by an order of 15%.

Figure 16 shows an instantaneous streakline view obtained through the TRPIV experiments. The “Turbulent-Non Turbulent” (TNT) and “Turbulent-Turbulent” shearing interfaces are clearly shown. By means of the morphing, the TT interface is lowered comparing to the static case and an associated benefit in the reduction of the suction effect as well as a slight dynamic increase of an “dynamic incidence” is obtained, related to the lift increase (figure 17 and Table 1).

The mean velocity fields (static and morphing), figure 17 show in zoom the reduction of the suction effect and therefore as known, reduction of the separated area (not captured by the PIV plane but induced), associated with the lift increase. They also show the slight increase of a downward effect of the near wake orientation also linked to the lift increase. Furthermore, a reduction of the wake’s width shown in this figure, provides *simultaneously* a drag reduction, (Table 1).

POD analysis of the experimental fields

Figure 18 shows the energy distribution according to the 40000 experimental snapshots, covering an order of 1280 vortex shedding periods. In the experimental case, the energy of the modes has been slightly increased as a function of the actuation frequency whereas it decreased beyond the 9th mode for the numerical case. A direct comparison is not easy to obtain, because the numerical duration is shorter than the experiments. Furthermore, the chaotic turbulence effects are modelled in case of the simulations whereas they are fully present in the experiments. This fact adds to the experimental POD a richer statistical content in the static and morphing cases than in the simulations. The PSD of the third POD mode (figure 19) shows formation of the VK predominant group of frequencies and its interaction with chaotic turbulence effects, creating a “spreading” of frequencies around this mode. The comparison with the actuation case at $210\,Hz$ shows a drastic decrease of the spectral energy and of the “bump” corresponding to the VK frequency. A significant drop of the spectral energy is shown in the intermediate frequency range thanks to the morphing and a decrease of the energy by 10 to 15 dB.

Figure 14. Tomo-PIV mean velocity field in the near wake (left: static, rigtht:morphing at f_a=300 Hz and Re=500,000 showing the reduction of the separated area by an order of 15%.

Figure 15. Mean velocity field, TRPIV results, $Re = 1 \times 10^6$. Left: static case, right: morphing at $f_a = 210\ Hz$. The vertical lines are located in respect to analysis of the shearing mechanisms on the corresponding mean velocity profiles, shown in figure 17.

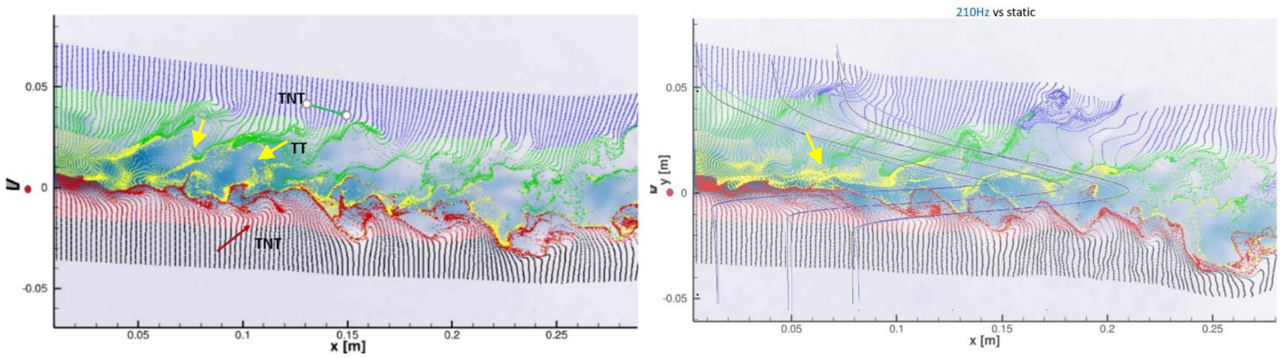

Figure 16. left: streaklines from the TRPIV results in the static case showing the Turbulent-Non Turbulent (TNT) interfaces, green and red, as well as the Turbulent-Turbulent (TT) interface (yellow). The red dot indicates the trailing edge position. Right: morphing at $f_a = 210\,Hz$ and visualization of the three mean velocity profiles indicated by the vertical lines in figure xxx. Illustration of the lowering of the TT interface downwards in the near trailing edge region and the benefits on the velocity profiles.

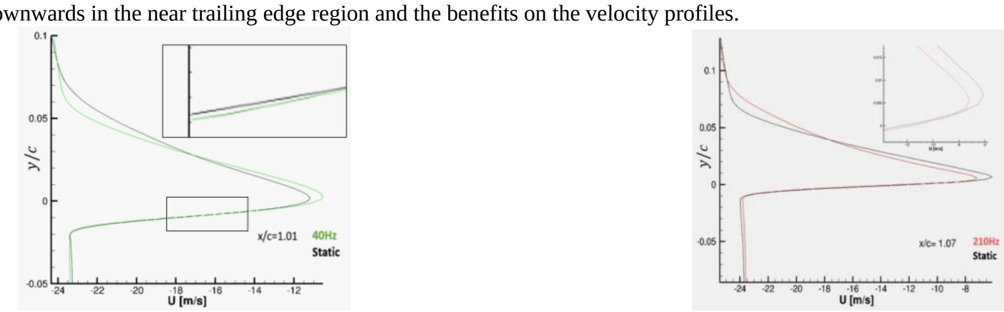

Figure 17. Vertical velocity profile at x/c=1.01and 1.07. Comparison of the static to morphing case at $f_a = 210\ Hz$. The zoom shows the velocity deficit decrease and the lower shift of the profile related to the lift increase. The narrowing of the profiles is related to simultaneous drag reduction evaluated in Table 1.

$f_a\ [Hz]$	40	70	80	130	160	210	260	300
$\frac{\overline{CL}_a - \overline{CL}_{static}}{\overline{CL}_{static}} \times 100$	+0.42	**+1.28**	+0.13	-1.62	-1.0	+0.6	+0.46	+0.4
$\frac{\overline{CD}_a - \overline{CD}_{static}}{\overline{CD}_{static}} \times 100$	**-5.0**	-1.0	**-4.0**	+2.4	+1.4	-0.4	-2.0	-1.9
$\frac{(\overline{CL}/\overline{CD})_a - (\overline{CL}/\overline{CD})_{static}}{(\overline{CL}/\overline{CD})_{static}} \times 100$	**+5.9**	+2.35	**+4.3**	-3.9	-2.4	+1	+2.5	+2.4

Table 1. Aerodynamic performance versus vibration frequency. Percentages of the force (drag and lift) modification through morphing, comparing to static case. Optimal performance (L/D ratio) for actuations of 40 Hz and 80 Hz, being sub-harmonics of the VK mode.

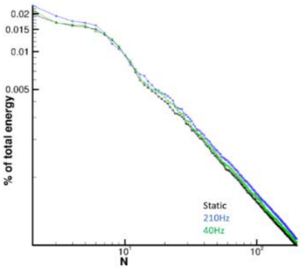

Figure 18. Energy diagram of the experimentally obtained POD modes versus the mode order (N).

Figure 20 shows the POD reconstruction (beyond the first mode), by considering the intermediate range of (20-60) modes. The eddy-blocking effect is clearly illustrated. Figure 21 shows the phase-averaged vorticity reconstruction according to the method described in the previous section. A comparison between the static and morphing vorticity fields at a phase angle near 320° is shown, indicating the shear layers constriction in the near region.

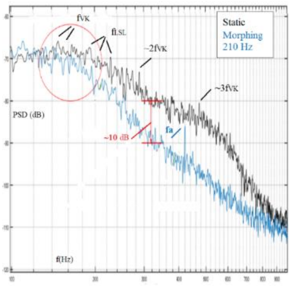

Figure 19. PSD of the 3rd POD-mode temporal coefficient showing drastic reduction of spectral energy thanks to morphing. Red ellipsis corresponds to VK natural frequency bump in the range of 150-160 Hz and its harmonics. Area near 210 Hz corresponds to lower shear layer natural frequency. Actuation with an equal frequency produces the spectral energy reduction.

CONCLUSIONS

This study presents a detailed analysis of the electroactive morphing effects on the aerodynamic performances of an A320 morphing wing prototype at Re= 1M, regarding the related physical mechanisms in the shearing regions of the separation and the near wake. The study has been conducted experimentally and numerically using the same parameters. The coherent structure dynamics have been simulated in agreement with the experimental flow physics. The simulations allowed for evaluation of optimal ranges of the morphing parameters, regarding the choice of amplitude and vibration frequency applied through a number of MFC piezo-actuators in the trailing-edge area along the span. Principal physical mechanisms governing the shear layers past the separation and in the near wake have been discussed and linked to the obtained aerodynamic performances. A lift increase in the order of **8%** has been obtained numerically and an increase of the aerodynamic efficiency (lift-to-drag ratio) in the order of **6%** experimentally, together with a decrease of drag by **5%** in the low actuation range (40 Hz). Specific actuation cases allowed for a *simultaneous* drag reduction and increase of lift thanks to the present morphing concept together with a reduction of the turbulence spectral energy concerning the main instability modes, by a **10%** to **15%** dB thus reducing the noise sources related to the noise propagation downstream of the trailing edge. The related physical mechanisms explaining these performances have been illustrated and emphasized through POD analysis, providing a detailed view of the modification in the shear layer dynamics thanks to the morphing.

REFERENCES

J.Abou Khalil, C. Jiménez Navarro, R. El Jeaid. A. Marouf, R. El Akoury, Y. Hoarau, J-F. Rouchon, M. Braza. (2024), Int. J. Num.

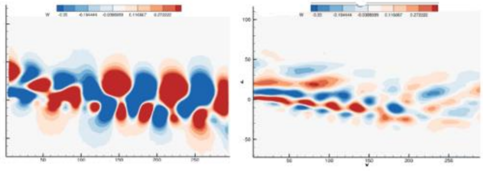

Figure 20. POD reconstruction between the 20-60 modes, top: static; bottom: morphing at 210 Hz.

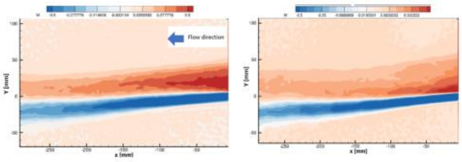

Figure 21. Phase averaged fields at a phase angle ϕ near 320°.

ACKNOWLEDGEMENTS

The present study has been partly funded by the Horizon 2020 N°723402 EU project SMS, “Smart Morphing & Sensing for aeronautical configurations” and partly from the French ANR - “Agence Nationale de Recherche” project EMBIA - “Electrical Multiscale Bio-inspired Live-skin interfaces in Aeronautics”, both coordinated by M. Braza at IMFT. The CPU allocation has been provided by the French Supercomputing Centers CINES, TGCC and CALMIP. The funding for the PhD of Clément Rouaix and the post-doc of Mateus Carvalho, co-supervised by Horia Hangan and Marianna Braza was provided by a CRC-Tier 1.

Meth. Heat & Fluid Flow, Vol. ahead of print, ISSN: 0961-5539,

G. Berkooz, P. Holmes, J.L. Lumley, Ann. Rev. Fluid Mech., 1993,.**25**, pp.539-575.

R. Bourguet, M. Braza, G. Harran, R. El Akoury, (2008), *J. Fluids and Structures*, **24** (8),1240-1251, 2008,

M. Braza, F. Auteri, P. Flaszynski, J.F. Rouchon, G. Tzabiras. 2023, **153,** *Notes on Num. Fluid Mech. and Multidiscipl. Design*, Springer, https://doi.org/10.1007/978-3-031-22580-2

M. Braza, R. Perrin, Y. Hoarau, *J. Fluids and Struct.*, **22**, pp. 757–771, 2006.

M. Braza, D. Faghani, H. Persillon (2001) *J. Fluid Mech.*, **439**, pp. 1-41.

C.B. Da Silva, J.C.R. Hunt, I. Eames, J. Westerweel, 2014. Ann. Rev. Fluid Mech. 46, 567–590.

J. Donea. S. Giuliani, J.P. Halleux, 1982. Comp. Meth. in Appl. Mech. &Eng. **33**, 689–723.

W. Haase, M. Braza, A. Revell, (2009), *Notes on Num. Fluid Mech. and Multidiscipl. Design*, **103**, Springer, ISBN 978-3-540-92772-3, 2009.

Y. Hoarau, D. Pena, J. B. Vos, D. Charbonier, A. Gehri, M. Braza, T. Deloze, E. Laurendeau, 54th AIAA Aerospace Sciences Meeting, (2016), San Diego, https://arc.aiaa.org/doi/abs/10.2514/6.2016-2056

G. Jodin, V. Motta, J. Scheller, E. Duhayon, C. Döll, J.F. Rouchon, M. Braza, (2017) *J. Fluids and Struct*,, **74**, pp. 263-290

A.Marouf, PhD thesis 2020, https://theses.fr/2020STRAD025

R. Perrin, PhD thesis 2005. https://oatao.univ-toulouse.fr/7270/

J. Scheller, PhD Thesis, (2015), https://www.theses.fr/189548525

J. Scheller, G. Jodin, K.J. Rizzo, E. Duhayon, J-F. Rouchon, M. Triantafyllou, M. Braza, *Solid-State Phenomena*, **251**, pp.106-112, 2016.

N. Simiriotis, PhD Thesis INPT, (2020), http://www.theses.fr/2020INPT0041

N. Simiriotis, G. Jodin, A. Marouf, P. Elyakime, Y. Hoarau, J.C. Hunt, J.F. Rouchon, M. Braza, *J. Fluids and Struct*, **91**, 2019.

Sirovich, L. (1987), *Quar. Appl. Math.*. **45**. 10.1090/qam/910463.

D. Szubert, F. Grossi, A. Jimenez-Garcia, Y. Hoarau, J. Hunt, M. Braza *J. Fluids and Struct*, **55**, pp. 276–302, (2015),

J.B. Tô, N. Simiriotis, A. Marouf, D. Szubert, I. Asproulias, D.M. Zilli, Y. Hoarau, J.C.R. Hunt, M. Braza, *J. Fluids and Struct.* 2019, **91**.